Discovery of Neptune's Inner Moon Hippocamp† with the Hubble Space Telescope

M. R. Showalter[1*], I. de Pater[2*], J. J. Lissauer[3*] & R. S. French[1*]

[1]SETI Institute, 189 Bernardo Avenue, Mountain View, CA 94043, USA.
[2]Department of Astronomy, University of California, Berkeley, CA 94720, USA.
[3]NASA Ames Research Center, Moffett Field, CA 94035, USA.

During its 1989 flyby, the Voyager 2 spacecraft imaged six small, inner moons of Neptune, all orbiting well interior to large, retrograde moon Triton[1]. The six, along with a set of nearby rings, are probably much younger than Neptune itself. They likely formed during the capture of Triton and have been fragmented multiple times since then by cometary impacts[1,2]. Here we report on the discovery of a seventh inner moon, Hippocamp, found in images taken by the Hubble Space Telescope (HST) during 2004–2016. It is smaller than the other six, with a mean radius *R* ≈ 16 km. It was not detected in the Voyager images. We also report on the recovery of Naiad, Neptune's innermost moon, seen for the first time since 1989. We provide new astrometry, orbit determinations, and size estimates for all the inner moons to provide context for these results. The analysis techniques developed to detect such small, moving targets are potentially applicable to other searches for moons and exoplanets. Hippocamp orbits just 12,000 km interior to Proteus, the outermost and largest of the inner moons. This places it within a zone that should have been cleared by Proteus as the larger moon migrated away from Neptune via tidal interactions. We suggest that Hippocamp is most likely a fragment of Proteus, providing further support for the

---

† Note to editor and reviewers: The name "Hippocamp" was recently approved by the IAU but has not yet been publicly announced. The designation "Neptune XIV" is expected to be approved during the IAU General Assembly in mid-August.

*e-mail: mshowalter@seti.org; imke@astron.berkeley.edu; jack.lissauer@nasa.gov; rfrench@seti.org

hypothesis that the inner Neptune system is relatively young and has been shaped by numerous impacts.

Hippocamp, also designated S/2004 N 1 and Neptune XIV, was discovered in 2013 during a re-analysis of lengthy HST exposures of the Neptune system[3]. We found it in images taken during 2004–2005 and 2009. HST images obtained in 2016 confirm the discovery (Fig. 1).

The long delay between image acquisition and discovery arose because of the specialized image processing techniques required. To detect a small moon in an image, motion smear should be limited to the scale of the point spread function (PSF). Neptune's inner moons orbit at speeds up to 12 km/s, whereas the projected scale of Hubble's PSF is a few thousand km; this limits exposure times to 200–300 s before smear dominates and signal-to-noise ceases to grow. However, using HST's widest filters, the detection of an object such as Hippocamp, with V magnitude ~ 26 [3], requires ~ 30 minutes of continuous integration, which is far longer than the smear limit. Thus, it might appear that HST is incapable of detecting such a faint, moving target.

We addressed this problem by introducing a distortion model to the Neptune images. Our procedure was to derive a pair of functions $r(\mathbf{x})$ and $\theta(\mathbf{x})$, which return orbital radius and inertial longitude as a function of 2-D pixel coordinate $\mathbf{x}$. The inverse function $\mathbf{x}(r,\theta)$ could also be readily defined. We derived the mean motion function $n(r)$ from Neptune's gravity field including its higher moments J_2 and J_4 [4]. One can use these functions to transform an image taken at time t_0 to match the appearance of another image at a time Δt later by relocating each pixel $\mathbf{x}_0$ in the original image to a new location $\mathbf{x}_1$:

$$\mathbf{x}_1 = \mathbf{x}(r(\mathbf{x}_0),\ \theta(\mathbf{x}_0) + n(r(\mathbf{x}_0)) \times \Delta t)\ . \qquad [1]$$

This transformation makes it possible to distort a sequence of images so that they all match the geometry of one frame; any moon on a prograde, circular, equatorial orbit will appear at fixed pixel coordinates. After the transformations, the images can be coadded so that much longer effective exposure times are obtained. Fig. 2 illustrates the technique. This procedure, originally developed to study Neptune's arcs, revealed Hippocamp. (Note that this procedure neglects the sub-pixel correction for each moon's Laplace plane; that topic is discussed further below.)

The geometric transformation creates a spiral pattern that winds tighter with decreasing r. (Fig. 2c). The method fails when adjacent pixels sheer to the point that individual PSFs become severely distorted. For the inner moons of Neptune, this limits the coadding of images to those that have been obtained within the same HST orbit. The total available integration time in one HST orbit is ~ 30 minutes, meaning that Hippocamp is just above the theoretical limit of what HST can detect in the inner Neptune system. The supplemental data for this paper includes all of the images used in this investigation at various levels of processing. The supplemental video shows one sequence of images in which Hippocamp is visible to the eye without distortion or coadding.

This same image analysis technique has also revealed Naiad (Extended Data Fig. 1). Identifying Naiad was challenging because its orbit differed substantially from that predicted by the latest reference ephemeris[5]; in 2016, Naiad falls nearly 180° away from its predicted location. Nevertheless, the astrometry from HST and Voyager is consistent with uniform, near-circular motion if one allows for a one-sigma increase in Naiad's Voyager-derived mean motion[6]; see Extended Data Table 1. The very large ephemeris error implies that reported detections of Naiad from the W. M. Keck Telescope in 2002[7] were misidentifications. A 20° error in the predicted orbit of Thalassa[5] suggest that it may also have been misidentified in the same data set.

Determining the orbits of Hippocamp and Naiad entailed solving simultaneously for the orbits of all Neptune's inner moons. Table 1 lists all our derived orbital elements: n = mean motion; a = semimajor axis; e = eccentricity; i = inclination; λ_0 = mean longitude at epoch; ϖ_0 = longitude of pericenter at epoch; Ω_0 = longitude of ascending node at epoch; ϖ' = apsidal precession rate; Ω' = nodal regression rate. Each orbit is defined relative to its local Laplace plane; this plane nearly aligns with Neptune's equator for the innermost moons, but tilts toward the plane of Triton's orbit for larger a. The calculated angle of this tilt, ψ, is listed in Table 1. All of the Laplace planes share a common ascending node, which coincides with the descending node of Triton's orbit.

Supplementary Table 1 lists all the images used in this analysis. Extended Data Tables 2–4 and Supplementary Table 2 contain all of our astrometry. Orbits have been determined only from HST data 2004–2016; for moons other than Hippocamp, more precise orbits could be obtained by also including prior detections from Voyager- and Earth-based telescopes[8]. Nevertheless, our orbital elements for the four largest moons are in extremely close agreement with prior determinations[4–6]; see the Methods section and Extended Data Table 4 for further details.

Table 1 also lists the disk-integrated photometry of Neptune's inner moons as obtained through broad visual filters. Again, our results agree with earlier Voyager and HST photometry[9]. The other inner moons all have albedos in the range 0.09 ± 0.01[9], so if Hippocamp's albedo is similar, then $R = 16 \pm 1$ km. Our photometry does not have sufficient accuracy to constrain the moon's shape or phase function.

We can rule out the existence of any additional moons interior to the orbit of Proteus that are more than half as bright as Hippocamp. Beyond the orbit of Proteus, our images are freer from Neptune's glare and orbital motion is slower, making it possible to add together larger sets of images (Extended Data Fig. 2). Implant tests within these images indicate that a moon ~ 30% as bright as Hippocamp would generally be visible beyond Proteus, but none have been seen. Our orbital coverage is generally complete out to $a \approx 200{,}000$ km and about 2/3 complete out to $a \approx 300{,}000$ km. Our search for retrograde, equatorial moons also yielded negative results.

We can extrapolate the orbit of Hippocamp back to the time of the Voyager 2 flyby (August 25, 1989) with a precision of ± 1.5° in orbital longitude. This information, combined with knowledge of Voyager's trajectory and its camera pointing, enabled us to identify where the moon might have appeared in the Voyager images. The orbital uncertainty corresponds to a few tens of pixels in images from the narrow-angle camera. Extended Data Table 5 lists the most sensitive candidate images. All are clear-filter images taken by the narrow-angle camera. Any prediction that fell within 200 pixels of the field of view is listed. This same procedure accurately predicted all the best images of Neptune's other inner moons. All candidate images are either badly smeared or definitively missed Hippocamp based on the observed locations of known moons. In retrospect, Voyager's deepest exposures were reserved for studies of the rings and small moons near and inside Neptune's Roche limit; Voyager missed this moon primarily because it orbits too far from the planet to have been captured in the most sensitive searches.

The orbital elements of Table 1 make a search for orbital resonances in the system possible. We conducted an exhaustive search following methods previously applied to the Pluto system[10]. Our search accounted for all plausible Lindblad, eccentric and inclined corotation, and three-body resonances up to second order in (e, i) and with numeric coefficients ≤ 200. No resonances were identified.

The discovery of tiny Hippocamp contributes to our understanding of the history of Neptune’s inner system. Nearby Proteus is thought to be the only inner moon that has survived intact since Triton’s orbit circularized[2,11]. Unlike the other Voyager-discovered moons, Proteus orbits outside the synchronous radius (83,525 km), so tidal interactions with Neptune have caused it to migrate outward. The rate of migration is highly uncertain, but a model for the excitation of the inner moons’ inclinations[12] suggests that Proteus has migrated at least 8,000 km since it originated. If so, then Proteus started its life very close to, if not interior to, where Hippocamp is now. Hippocamp is too small to raise a significant tide on Neptune, so its orbit has remained fixed. Unless Neptune’s tidal quality factor is much smaller than previously inferred[12], these two moons must have had a very close interaction in the past.

Our preferred explanation is that Hippocamp arose from an impact into Proteus. Neptune’s smaller moons have likely been disrupted numerous times in the past[1,2], whereas a large crater on Proteus suggests that it came close to disruption[11]. After the impact, Proteus continued its outward migration but the impact debris did not; eventually that debris accreted into the moon we see today. Hippocamp may have been broken apart multiple times afterward but, owing to its relative isolation from the rest of the system, most of the same material quickly re-accreted back into the same moon at the same location. Proteus would probably have pumped up Hippocamp’s eccentricity while the two moons were still nearby, but even a single breakup event would leave the moon on the low-eccentricity orbit where we find it today. Thus, the existence of Hippocamp dramatically illustrates the battered history of Neptune’s inner system.

METHODS

Data Selection: Our data set encompasses most of HST's images of the Neptune system obtained during 2004–2016. Only our own observing programs (GO-10398, 11656, and 14217) were capable of detecting Hippocamp, but the others provided detections of the larger moons, which contributed to the precision of our orbit solutions and photometry. Three programs that focused exclusively on imaging the planet through narrowband filters (GO-10423, 14044, and 14334) were omitted because of low sensitivity to the small satellites. Supplemental Data Table 1 lists all of the images we analyzed for this investigation. We performed all of our analysis using calibrated ("FLT") image files.

Observing Techniques: For our own observing programs, all images were targeted at the center of Neptune. On some occasions, we performed dithering steps part way through an orbit of HST in order to prevent hot pixels from remaining at fixed locations. However, we found this not to be strictly necessary; the moons move by many pixels within a single HST orbit, so no moon is ever affected by a hot pixel more than once. We limited exposure times to ~ 300 s and generally used the widest available filters.

Most observations were scheduled to keep Triton outside the field of view. However, this was not always possible, and as can be seen in Table 1 and Supplemental Data Table 2, observations of Triton contributed to our analysis, in particular because the orbit of Triton defines the orientation of the Laplace planes.

During 2004 (program GO-10398; see Fig. 1a), we used the occulting mask on the High Resolution Channel (HRC) of the Advanced Camera for Surveys (ACS) to suppress excess light from Neptune. Although the mask was designed to obscure point targets, we found it quite successful at suppressing the glare from Neptune. The 3″ mask only barely covered Neptune's 2.4″ disk, requiring us to center Neptune with fine precision. The process of positioning the coronagraph is automated; the camera takes an image and then shifts the pointing to place the brightest pixel at the center of the mask. We found that Neptune is a featureless disk in ultraviolet light and so used filter F330W for the initial pointing. This procedure worked every time.

We also developed other techniques to suppress the light from Neptune in the absence of a coronagraph. The CCDs on HST "bloom" along the y-axis when saturation occurs, but this generally does not corrupt pixels that are offset along the x-axis. During 2005 (Fig. 1b) we simply shortened our exposure times to limit the distance over which the bloom would occur. In 2009 and 2016 (Figs. 1c,d) we chose observing periods around opposition, when we could orient the camera with the rings and satellites along the x-axis. In these cases, severely overexposing Neptune is essentially harmless.

Image Processing: Although we were able to control Neptune's saturation using the methods described above, glare from Neptune was ever-present and, as with all long exposures on HST, cosmic ray hits created a smattering of "snow" atop most images (Extended Data Fig. 3a). Hot pixels fall at known locations in each image and are cataloged for each detector. Cosmic ray hits were recognized as clusters of pixels in one image that differ by more than three standard deviations from the median of identical exposures from the same HST orbit. For cosmetic purposes, we overwrote these pixels with the median of the adjacent pixels (Extended Data Fig. 3b). However, we also kept track of overwritten pixels using a boolean mask and ensured that masked pixels were ignored in the subsequent data analysis (Extended Data Fig. 3c). We handled the glare and diffraction by aligning the center of Neptune in all the images from each HST visit that shared a common filter. We constructed a reference image from the median value among all the pixels after aligning on the center of Neptune. Unlike the mean, the median is not affected by moons (which move rapidly) or cosmic ray hits (which are transient). The resulting reference images were therefore a smooth representation of Neptune's glare and diffraction spikes. Subtracting the reference yielded individual images that were almost free of distracting background gradients (Extended Data Fig. 3d).

The specific processing steps we performed were always adapted to the scientific goals. For astrometry of all but the smallest three moons, we worked with unprocessed images because we did not want to corrupt the PSF and because we could handle the glare as part of our modeling. For Naiad, Thalassa, and Hippocamp, all of the above steps were required because the most important consideration was to maximize visual detectability (Figs. 1 and 2; see Extended Data Tables 1–3).

Small Moon Detections: The three smallest moons, Naiad, Thalassa and Hippocamp, required additional effort to detect. We performed a procedure akin to "unsharp mask", in which we subtracted the median of the nearby pixels (in a box ranging in size from a 7×7 to 13×13, depending on the circumstances) from each pixel in a given image. Normally, unsharp masking uses the mean, not the median, but the median suppresses most of the artifacts produced by the mean, such as creating dark circles around bright features. This step removed the last remaining background gradients from the images (Extended Data Fig. 3e).

We customized the image distortion and coadding procedure for each moon, based on the number of images required to obtain a usable detection. Hippocamp always required the coadding of an entire HST orbit. Naiad could often be detected in half-orbits of coadded data; this allowed us to obtain two measurements per HST orbit rather than one. Thalassa could sometimes be seen in individual images, but in other cases it was necessary to coadd two or more images. We described our coadding procedure above (Fig. 2). Once we detected a body, we adopted a slightly different image processing procedure to optimize the images for our analysis. That was to transform each set of images using a fixed mean motion n_m matched to moon m's mean motion as inferred during the discovery/recovery process:

$$\mathbf{x}_1 = \mathbf{x}(r(\mathbf{x}_0),\ \theta(\mathbf{x}_0) + n_\mathrm{m} \times (t_1\text{-}t_0)) \qquad [2]$$

This transform is preferred because it does not create a spiral pattern that arises when n is treated as a function of r, so it is less disruptive to the PSFs.

When searching for moons outside of Hippocamp and Proteus, motion is slow enough that we could coadd images spanning a few adjacent orbits. In these cases, we transformed the images using polar coordinates, so that the longitude at epoch varies from 0 to 360° along the horizontal axis and radius increases along the vertical axis:

$$r_1 = r(\mathbf{x}_0) \qquad [3a]$$

$$\theta_1 = \theta(\mathbf{x}_0) + n(r(\mathbf{x}_0)) \times \Delta t \qquad [3b]$$

Astrometry: Because Neptune is large and/or often saturated, is was unusable as a pointing reference. Background stars could have also provided pointing references but these are generally absent. As a result, we performed an initial navigation (pointing correction) for each image by searching for the brightest moons (Larissa, Proteus, and Triton) by eye. We could easily obtain initial precision of 1–2 pixels, at which point it became practical to search for the known moons using an automated procedure. However, all detections were inspected visually and rejected if the moon could not be clearly seen or if something nearby might have corrupted the measurement. Naiad, Thalassa, and Hippocamp were too small to be detected in this way and were handled by an entirely manual process, as discussed further below.

For each measurement, we fitted a model point spread function (PSF) to a small square of the image surrounding each detectable body. Model PSFs were generated using the "Tiny Tim" software maintained by the Space Telescope Science Institute (STScI)[13]. The parameters to be fitted included the center position (x, y), the scaling factor to match the brightness of the body, and parameters to define an underlying 2-D ramp of background light. The background ramp was needed to account for Neptune's glare. Nearest the planet, we used a 2-D quadratic requiring six additional free parameters; elsewhere, we used a 2-D linear function requiring just three.

For the faintest moons, we adopted a slightly different procedure. Many of these images had been distorted and coadded, so the PSF was no longer accurately described by the Tiny Tim model. Instead we used a uniform 2-D gaussian to describe the PSF. Given how faint these objects are in our data, this simpler PSF model was adequate to our needs.

We solved for the best-fit values of (x, y) via straightforward nonlinear least-squares fitting (Extended Data Tables 1–3; Supplemental Data Table 2). We estimated the uncertainties by linearizing the model around the best-fit solution and then solving for the covariance matrix. On average, this procedure provided a reliable estimate of the uncertainties of the brighter moons, but appears to have provided an underestimate for the faintest targets (Table 1). However, by statistical chance, sometimes error bars were clearly too small; this created difficulties when we started fitting orbits because the measurements, although extremely accurate, produced anomalously large residuals in units of the uncertainty. We solved this problem later by setting 0.1 pixels as the absolute floor for all measurement uncertainties.

Orbit Models: We describe the orbit of each moon using nine orbital elements (Table 1). However, we reduce the number of free parameters to six by using Neptune's known gravity field to derive the values of semimajor axis (a), apsidal precession rate (ϖ'), and nodal regression rate (Ω') from the mean motion n, eccentricity e, and inclination i. The relationship we used is accurate to second order in (e, i)[14]. We used GM = 6835100 km^3/s^2; $J_2 = 3408.43\times10^{-6}$; $J_4 = -33.40\times10^{-6}$, assuming Neptune's radius is 25,225 km[4]. Our reference epoch is midnight 2009 January 1 UTC, chosen because it falls near the mid-time of all our observations. In Barycentric Dynamical Time, this is 284,040,066.184 seconds after the J2000 epoch (2000 January 1.5 TDB).

Triton's orbital inclination is 157.4°, meaning that it is both retrograde and tilted away from Neptune's equator by 22.6°. Its nodal regression period is approximately 600 years. Over that interval, the pole of Triton's orbit sweeps out a cone of half-width 22.2° while Neptune's rotation pole sweeps out a cone of 0.5°. This polar wander is rapid enough that it must be accounted for when describing the orbits of the inner moons. Furthermore, Triton tilts the Laplace planes of the moons away from Neptune's equator and toward its own orbital plane. We follow methods described elsewhere[6] to determine the tilt of each moon's Laplace plane (Table 1).

Note that, for Triton's orbit, we described the shape and orientation using prograde angles, but then reverse the signs of n, ϖ', and Ω'. Furthermore, we held n, a, and Ω' fixed in our analysis but used our own astrometry to define the remaining elements. We chose this approach because (a) our time baseline for Triton was quite short compared to previous studies[4], (b) these quantities define the orientation of the Laplace plane, which affects all the remaining moons, but (c) vagaries in the definition of the longitude reference (discussed below) left us uncomfortable depending entirely on the published orbital elements[4]. However, our results were quite compatible with previous results; see Extended Data Table 4.

Defining an appropriate reference longitude in the context of all these misaligned planes and precessing poles is challenging. Ideally, we seek an inertially fixed definition that is independent of epoch. Notably, previous papers on the orbits of Neptune's inner moons have adopted many different references, none of which meet these requirements. The common node of all the Laplace planes is a tempting reference point, but it is not well determined and, of course, it rotates every 600 years. For this investigation, all longitudes are measured from the ascending node of the Neptune system's invariable plane on the ICRF (International Celestial Reference Frame) equator.

This is a by definition a fixed direction in space. The pole of this plane has right ascension 299.46 ± 0.14° and declination 43.40° ± 0.03° [4]. The uncertainties are small; any future change in the best-fit invariable pole will merely introduce a small, constant offset to the orbital elements λ_0, ϖ_0, and Ω_0. From this reference direction, all longitudes are measured as broken angles along the invariable plane to the common ascending node of all the Laplace planes, thence along each moon's Laplace plane to its orbital ascending node, and thence along the orbit plane. Using this new frame definition, we can update all published orbital elements to a common epoch (Extended Data Table 1). All orbits are in good agreement for Despina, Galatea, Larissa, and Proteus. The orbit of Naiad agrees between this work and the Voyager-era solution[6] if one increases its mean motion by one standard deviation; the 2004 solution[5] disagrees with this work because it includes an erroneous measurement. We also note that the orbit solutions for Thalassa appear to be diverging, although all solutions agree at the Voyager epoch.

Orbit Fitting: We converted our astrometry from (*x, y*) coordinates to right ascension and declination using the published distortion models for the HST cameras[15]. In the case of images taken using the unsupported CLEAR filter on ACS/HRC, later analysis showed persistent, large residuals. By experimentation, we determined that this was caused by a plate scale error; a scale correction factor of 0.9987 made the problem go away.

The fitting process requires a simultaneous solution for the orbital elements of every moon plus the precise navigation of every image. As in previous analyses of HST images[10,16], we have assumed that HST does a perfect job of tracking the position of Neptune within each HST orbit. Thus, one need not determine a unique pointing correction for every image; instead, images obtained through the same filter during a single HST orbit can reliably share a common navigation. Images taken through different filters are navigated independently, however, because the optical paths are different and shifts of up to 0.5 pixels were sometimes noted. Supplemental Data Table 1 lists, for every image, the reference image to which its navigation was tied.

Our initial analysis focused on the five best-observed moons: Despina, Galatea, Larissa, Proteus, and Triton. Because the parameters describing image navigations and those describing the orbits are only weakly coupled, it was practical to fit the orbits and navigate the images via iteration. First, we would solve for the orbital elements of all five moons while holding the navigations fixed. Second, we held the orbits fixed and solved for improved navigations. Repeating the process quickly led to convergence for both sets of parameters. Most navigations were quite precise; the median uncertainty was 0.01 pixel and the mean was 0.05. At each iteration, we used the best-fit determination of Triton's descending node to define the ascending node of the Laplace planes for the other moons. After this process completed, we held the navigations fixed while solving for the orbits of the smaller moons.

Not unexpectedly, this analysis revealed that a small number of our measurements were erroneous. We categorized each measurement by its linear distance d from the predicted position of the moon in units of its uncertainty. We categorized measurements with $d < 4$ as valid and those with $d \geq 8$ as clearly invalid. Invalid measurements were rejected outright, whereas measurements with $4 \leq d < 8$ were regarded as ambiguous. Including them in the fit could allow erroneous measurements to bias our answers, but excluding them would artificially reduce our assessment of the uncertainties. Our solution was to exclude them from the fit, but then to apply an enhancement factor to the overall goodness of fit (GOF) following a procedure to compensate for the possible bias[10].

Photometry: We obtained raw photometry from individual images by summing the pixel values inside squares centered on the known location of each moon. We measured each moon using multiple squares spanning a large range of sizes, generally from 5 to 25 pixels, always in odd numbers. For each square, we used the pixels of the outer border, one or two pixels wide, to define a background level, which we then subtracted from the remaining, interior pixels.

Making measurements within a small sets of pixels always results in an undercount of the reflected sunlight because the PSF has extended tails. However, we performed the same analysis on the theoretical PSFs generated by Tiny Tim[13] to determine the expected shortfall, and then applied the appropriate correction factor to each measurement. The optimal size of each square depends on circumstances; smaller squares provide less precision because of small numbers of pixels and because the correction factor is large, but large squares can be easily corrupted by background variations and/or bad pixels. Afterward, we merged all sets of measurements of the same moon from the same HST orbit and filter, and then we applied statistical tests to recognize and omit the outliers. Results are shown in Table 1.

We convert from raw image values to the calibrated, disk-integrated reflectivity as follows. The file header of every calibrated Hubble data product contains a parameter value PHOTFLAM, the image's "inverse sensitivity" in units of erg/cm^2/Å/s. PHOTFLAM, multiplied by the exposure time, converts the numbers in the image array to intensity I in physical units of erg/cm^2/Å. Reflectivity is the dimensionless ratio of I to F, where πF is the incoming solar flux density. We calculate F by averaging the solar spectrum (as defined by STScI data product "sun_reference_stis_001.fits") over the throughput of each instrument and filter. The resulting value is as would be measured at 1 AU, so we correct it for the Sun-Neptune separation distance. The resulting factor would be appropriate to determine the reflectivity of an extended source such as Neptune itself. For an unresolved point source, we also multiply by the projected area of a pixel in units of km^2. The resulting quantity, when multiplied by the sum of the pixel values within the PSF of a point source, is the disk-integrated reflectivity $\int I/F\, dA$ that we seek (Table 1).

Data Availability

All source data used in this study is in the public domain and may be requested from the STScI archive at http://archive.stsci.edu/hst/search.php. The Voyager images referenced in this paper can be retrieved from NASA's Planetary Data System at https://pds-rings.seti.org/viewmaster/volumes/VGISS_8xxx/VGISS_8207. Data files representing most intermediate steps in the image processing can be found at http://dmp.seti.org/mshowalter/neptune_xiv.

Code Availability

Python 2.7 source code that implements all the key image processing steps can be found at http://dmp.seti.org/mshowalter/neptune_xiv/software. Orbit fitting and image geometry calculations are widely used procedures for which many implementations exist; we have documented all our procedures in detail but have not distributed our own custom source code.

1. Smith, B. A., Soderblom, L. A., Banfield, D., Barnet, C. et al. Voyager 2 at Neptune: Imaging Science results. *Science* **246,** 1422–1449 (1989).
2. Banfield, D. & Murray, N. A dynamical history of the inner Neptunian satellites. *Icarus* **99,** 390–401 (1992).
3. Showalter, M. R., de Pater, I., Lissauer, J. J. & French, R. S. NEW SATELLITE OF NEPTUNE: S/2004 N 1. CBET 3586 (2013).
4. Jacobson, R. A. The orbits of the Neptunian satellites and the orientation of the pole of Neptune. *Astron. J.* **137,** 4322–4329 (2009).
5. Jacobson, R. A. & Owen, W. M. The orbits of the inner Neptunian satellites from Voyager, Earth-based, and Hubble Space Telescope observations. *Astron. J.* **128,** 1412–1417 (2004).
6. Owen, W. M., Vaughan, R. M. & Synnott, S. P. Orbits of six new satellites of Neptune. *Astron. J.* **101,** 1511–1515 (1991).
7. Marchis, F., Urata, R., de Pater, I., Gibbard, S., Hammel, H. B. & Berthier, J. Neptunian satellites observed with Keck AO system. *Bull. Amer. Astron. Soc.* **36**, 860 (2004).
8. Brozovic, M., Showalter, M. R., Jacobson, R. A., French, R. S., de Pater, I. & Lissauer, J. Orbits of the inner satellites of Neptune. AAS/DDA meeting #49, 402.01 (2018).
9. Karkoschka, E. Sizes, shapes, and albedos of the inner satellites of Neptune. *Icarus* **162,** 400–407 (2003).
10. Showalter, M. R. & Hamilton, D. P. Resonant interactions and chaotic rotation of Pluto's small moons. *Nature* **522,** 45–49 (2015).
11. Croft, S. K. Proteus: Geology, Shape, and Catastrophic Disruption. *Icarus* **99**, 402–419 (1992).
12. Zhang, K. & Hamilton, D. P. Orbital resonances in the inner Neptunian system II. Resonant history of Proteus, Larissa, Galatea, and Despina. *Icarus* **193,** 267–282 (2008).
13. Krist, J. & Hook, R. The Tiny Tim User's Guide Version 6.3. http://tinytim.stsci.edu/static/tinytim.pdf (2004).
14. Renner, S. & Sicardy, B. Use of the geometric elements in numerical simulations. Celestial Mech. Dyn. Astron. **94**, 237–248 (2006).

15. Shupe, D. L. & Hook, R. N. The SIP Convention for Representing Distortion in FITS Image Headers. ASP Conference Series **XXX**, P3.2.18 (2005).

16. Showalter, M. R. & Lissauer, J. J. The second ring-moon system of Uranus: Discovery and dynamics. *Science* **311**, 973–977 (2006).

Acknowledgments Support for this work was provided by NASA through grant numbers HST-GO-10398, 11656, and 14217 from the Space Telescope Science Institute, which is operated by AURA, Inc., under NASA contract NAS 5-26555. Additional support for MRS and RSF was provided by NASA's Outer Planets Program through grant NNX14AO40G.

We thank Anthony Roman of STScI for his extensive support during the planning of the HST observations.

Author contributions MRS, IdP, and JJL are the co-investigators on the HST programs that led to the discovery of Hippocamp. MRS and RSF performed the data analysis and modeling effort. IdP provided additional data analysis methods that contributed to our interpretation of the results. JJL contributed the theoretical analysis and interpretation of the Neptune system's long-term evolution and the origin of Hippocamp. All authors contributed to the final version of the manuscript.

Competing interests The authors declare no competing interests.

Correspondence and requests for materials should be addressed to MRS.

Table 1 | Properties of Neptune's moons from HST data 2004–2016

	Naiad	Thalassa	Despina	Galatea	Larissa	Hippocamp	Proteus	Triton
n (°/day)	1222.858311	1155.758557	1075.733089	839.661310	649.054087	378.906239	320.765622	-61.257264
±	0.000169	0.000033	0.000012	0.000005	0.000004	0.000031	0.000001	0.000000
a (km)	48224.41	50074.44	52525.95	61952.57	73548.26	105283.56	117647.13	354759.00
e	0.0047	0.00176	0.00038	0.00022	0.00118	0.00019	0.00042	0.00036
±	0.0018	0.00054	0.00016	0.00008	0.00006	0.00038	0.00003	0.00008
i (°)	5.002	0.120	0.053	0.024	0.188	0.082	0.048	23.088
±	0.234	0.060	0.015	0.010	0.006	0.056	0.003	0.008
λ_0 (°)	156.206	50.821	315.642	351.111	47.808	325.135	351.304	-24.047
±	0.312	0.068	0.015	0.008	0.006	0.047	0.002	0.006
ϖ_0 (°)	315.981	230.598	227.125	222.434	43.620	4.932	270.620	104.038
±	20.510	17.795	23.462	20.648	2.708	118.773	3.115	9.693
Ω_0 (°)	165.949	195.879	254.777	197.458	99.641	28.429	45.145	2.567
±	2.595	29.708	15.674	19.108	1.787	34.781	3.078	0.029
ϖ' (°/day)	1.695099	1.507827	1.274838	0.714282	0.391340	0.111343	0.075456	-0.001097
Ω' (°/day)	-1.712177	-1.505873	-1.273331	-0.713675	-0.391111	-0.111311	-0.075448	0.001434
ψ (°)	0.0054	0.0066	0.0085	0.0198	0.0480	0.3078	0.5483	0.0000
N_1	15	50	231	316	349	18	409	38
N_0	1	2	10	14	10	1	2	1
DOF	24	94	456	626	692	30	812	71
GOF	1.56	1.47	1.08	1.01	1.02	1.50	0.93	0.79
RMS (″)	0.013	0.015	0.010	0.010	0.007	0.008	0.003	0.005
$\int I/F\,dA$ (km^2)	204.8	372.0	1367.1	1713.5	2112.9	59.0	10771.8	
±	37.1	28.8	65.9	32.0	20.4	5.6	58.9	
R (km)	30.2	40.7	78.0	87.4	97.0	16.2	219.0	
±	3.2	2.8	4.7	4.9	5.4	1.2	12.2	

Definitions: N_1 and N_0, are the number of weighted and unweighted measurements, respectively; DOF = degrees of freedom; GOF = goodness of fit, equal to $(\chi^2/\text{DOF})^{1/2}$; RMS = the root-mean-square residual of the measurements from the orbit model; $\int I/F\, dA$ = the disk-integrated reflectance, adjusted for a phase angle of 1°; R = the radius in km, assuming that the moon is a sphere with geometric albedo 0.09 ± 0.01 and has a phase function slope of 0.24 mag/degree[9]. Longitudes are measured starting from the ascending node of the Neptune system's invariable plane on the ICRF equator as described in the Methods section. For Triton, angles are measured in the prograde direction but motions are sign-reversed. The epoch is 2009 January 1 UTC.

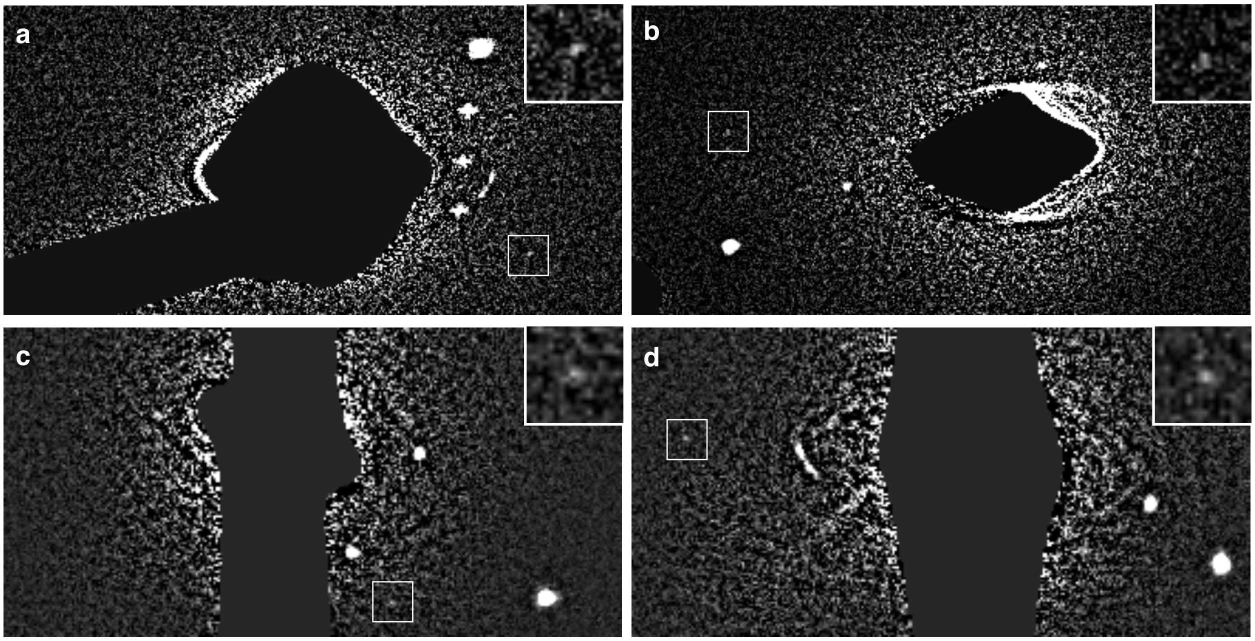

Fig. 1 | Detections of Hippocamp 2004–2016. Each panel shows a portion of an HST image after processing and coadding as described in the text. A small square locates Hippocamp in each panel; a closeup is inset at upper right. **a**, View from Visit 04 of HST program GO-10398, showing the earliest detection of Hippocamp on 2004 Dec 9. Neptune is behind the HRC occulting mask. **b**, View from Visit 08 of GO-10398, taken on 2005 May 12. **c**, View from the first orbit from Visit 01 of GO-11656 on 2009 August 19. The gray vertical band is due to Neptune's saturation bloom. **d**, View from the first orbit of Visit 03 of GO-14217 on 2016 Sep 2. Panels **a** and **b** have been rotated 90° counterclockwise.

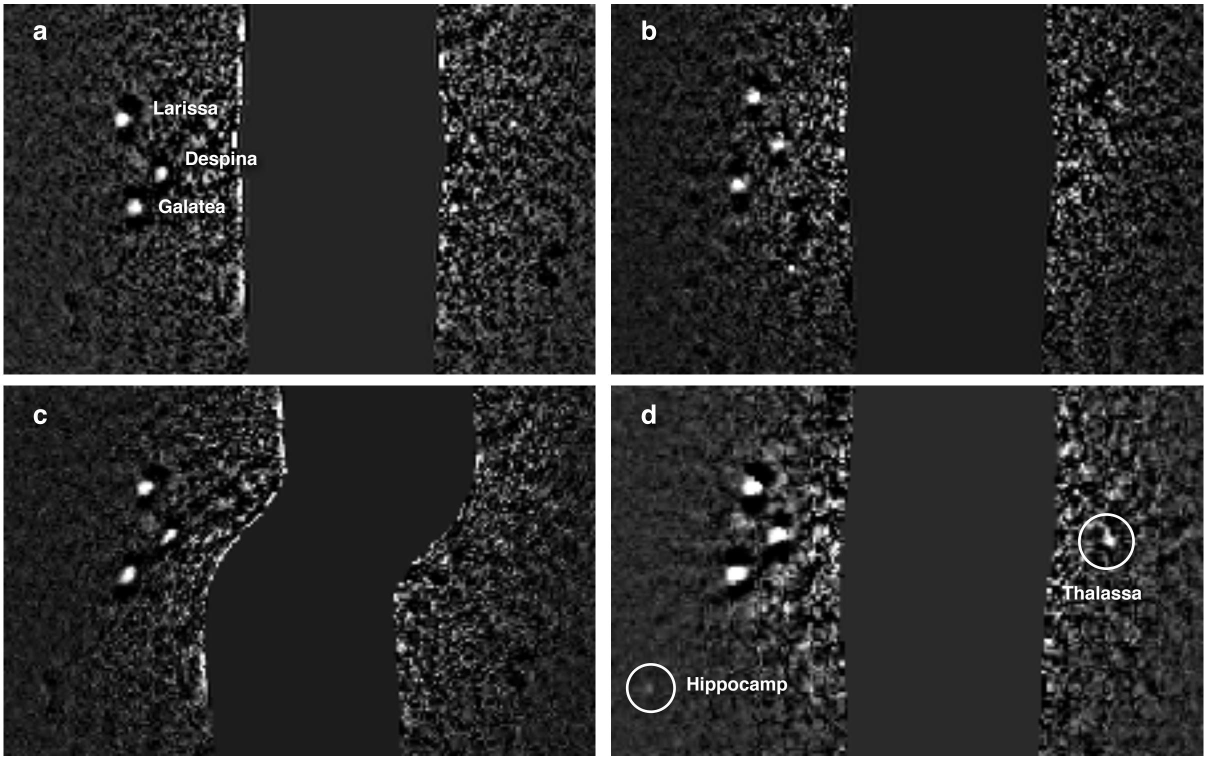

Fig. 2 | Image processing steps leading to the discovery of Hippocamp. a, Image ib2e02ziq_flt, the first in a sequence of eight long exposures from the second HST orbit of Visit 02 in program GO-11656 (2009 August 19). **b**, Image ib2e02zmq_flt, taken 21 minutes later. Despina, Galatea and Larissa have shifted noticeably in position. **c**, Image from panel **a**, transformed to match the geometry of the image in panel **b**. **d**, The result of coadding all eight images, revealing Hippocamp and Thalassa.

Extended Data Table 1 | Comparison of projected mean longitudes at three epochs

		As Published			Longitude Origin	1989 Aug 18.5 TDB	2000 Jan 1.5 TDB	2009 Jan 1.0 UTC
Orbit	**Reference**	**Epoch**	**λ (°)**	**n (°/day)**	**(°)**	**λ (°)**	**λ (°)**	**λ (°)**
Naiad	**O 1991 [6]**	1989 Aug 18.5 TDB	60.260	1222.844100	0.202	60.463	73.913	54.829
	±		0.042	0.013800		0.042	52.274	97.642
	JO 2004 [5]	1989 Aug 18.5 TDB	68.103	1222.843579	352.424	60.528	72.005	51.207
	±		0.035	0.000804		0.035	3.046	5.689
	This work	2009 Jan 1.0 UTC	156.206	1222.858311		61.288	128.571	156.206
	±		0.312	0.000169		1.235	0.637	0.312
Thalassa	**O 1991 [6]**	1989 Aug 18.5 TDB	239.737	1115.755600	0.202	239.939	322.152	329.542
	±		0.028	0.010100		0.028	38.259	71.463
	JO 2004 [5]	1989 Aug 18.5 TDB	247.581	1155.755977	352.424	240.005	283.646	32.306
	±		0.025	0.000236		0.025	0.894	1.670
	This work	2009 Jan 1.0 UTC	50.821	1155.758557		240.264	293.679	50.821
	±		0.068	0.000033		0.243	0.128	0.068
Despina	**O 1991 [6]**	1989 Aug 18.5 TDB	85.272	1075.734200	0.202	85.474	126.623	323.630
	±		0.014	0.002800		0.014	10.606	19.811
	JO 2004 [5]	1989 Aug 18.5 TDB	93.113	1075.733061	352.424	85.538	122.373	315.635
	±		0.014	0.000031		0.014	0.118	0.220
	This work	2009 Jan 1.0 UTC	315.642	1075.733089		85.346	122.288	315.642
	±		0.015	0.000012		0.084	0.041	0.015
Galatea	**O 1991 [6]**	1989 Aug 18.5 TDB	46.644	839.659800	0.200	46.845	78.167	340.403
	±		0.011	0.002500		0.011	9.470	17.689
	JO 2004 [5]	1989 Aug 18.5 TDB	54.488	839.661288	352.424	46.912	83.871	350.999
	±		0.010	0.000022		0.010	0.084	0.156
	This work	2009 Jan 1.0 UTC	351.111	839.661310		46.869	83.911	351.111
	±		0.008	0.000005		0.037	0.019	0.008
Larissa	**O 1991 [6]**	1989 Aug 18.5 TDB	184.828	649.053400	0.197	185.025	359.304	42.854
	±		0.009	0.001600		0.009	6.061	11.321
	JO 2004 [5]	1989 Aug 18.5 TDB	192.665	649.054076	352.424	185.090	1.929	47.701
	±		0.008	0.000013		0.008	0.050	0.092
	This work	2009 Jan 1.0 UTC	47.808	649.054087		185.117	1.999	47.808
	±		0.006	0.000004		0.027	0.014	0.006
Proteus	**O 1991 [6]**	1989 Aug 18.5 TDB	213.669	320.765400	0.136	213.805	273.140	349.639
	±		0.007	0.000900		0.007	3.409	6.368
	JO 2004 [5]	1989 Aug 18.5 TDB	221.446	320.765626	352.424	213.870	274.061	351.303
	±		0.006	0.000005		0.006	0.020	0.036
	J 2009 [4]	2000 Jan 1.5 TDB	274.037	320.765625	-0.037	213.814	274.000	351.236
	±							
	This work	2009 Jan 1.0 UTC	351.304	320.765622		213.899	274.076	351.304
	±		0.002	0.000001		0.010	0.005	0.002

The mean longitude of each Voyager-discovered moon is propagated to the epoch of each published solution. All are referenced to the zero longitude as defined in the Methods section. The origin column indicates the location in this frame of the published reference longitude used for that orbit; it must be added to the published solution to match the frame defined herein.

Extended Data Table 2 | Astrometry of Hippocamp used in this study

Reference image	Coadded images	*X*	*Y*	σ(*X*) (arcsec)	σ(*Y*) (arcsec)	ΔRA (arcsec)	Δdec (arcsec)	σ(RA,dec) (arcsec)	Weight	Significance σ
j95m01evq_flt.fits	3	419.905	983.383	0.245	0.279	-4.71083	-0.52989	0.00733	1	4.1
j95m03ifq_flt.fits	8	442.547	606.485	0.111	0.110	4.61133	1.11854	0.00310	1	1.9
j95m04o7q_flt.fits	8	415.309	614.063	0.125	0.143	4.18553	1.76370	0.00373	1	2.2
j95m04ogq_flt.fits	10	389.315	652.968	0.175	0.144	3.14446	2.27472	0.00454	1	8.0
j95m07zaq_flt.fits	10	529.582	331.713	0.196	0.197	-4.59685	-1.49436	0.00548	1	6.3
j95m08s6q_flt.fits	10	537.788	721.129	0.200	0.212	4.24118	2.00719	0.00576	0	7.0
j95m10dwq_flt.fits	10	559.793	694.247	0.191	0.209	3.45606	2.41926	0.00558	1	2.2
ib2e01vyq_flt.fits	8	225.503	204.913	0.187	0.200	1.94309	2.89358	0.00793	1	5.4
ib2e02z5q_flt.fits	8	159.003	212.849	0.294	0.293	-3.67239	0.43086	0.01202	1	7.8
ib2e02zmq_flt.fits	8	122.356	220.386	0.085	0.086	-4.54705	-0.79563	0.00400	1	10.3
icwp01n4q_flt.fits	5	375.252	273.108	0.167	0.167	4.33707	2.25391	0.00685	1	3.2
icwp01n9q_flt.fits	6	386.737	257.340	0.106	0.095	3.94597	3.01595	0.00412	1	13.1
icwp02blq_flt.fits	5	370.515	210.964	0.114	0.108	3.53570	3.23073	0.00455	1	6.9
icwp02bqq_flt.fits	6	348.150	203.908	0.190	0.188	2.32396	3.28502	0.00775	1	12.2
icwp03d4q_flt.fits	5	130.684	259.311	0.182	0.182	-4.33872	-2.33937	0.00746	1	5.2
icwp03d9q_flt.fits	6	134.071	269.453	0.111	0.115	-4.29122	-2.54452	0.00463	1	5.9
icwp03djq_flt.fits	5	132.473	282.774	0.121	0.119	-3.79819	-3.11456	0.00492	1	11.3
icwp03dqq_flt.fits	6	140.824	292.188	0.109	0.110	-3.59033	-3.20651	0.00449	1	6.7
icwp04ijq_flt.fits	5	320.172	207.120	0.339	0.335	0.99361	2.94336	0.01382	1	19.3

Extended Data Table 3 | Astrometry of Naiad used in this study

Reference image	Coadded images	*X*	*Y*	σ(*X*) (arcsec)	σ(*Y*) (arcsec)	ΔRA (arcsec)	Δdec (arcsec)	σ(RA,dec) (arcsec)	Weight
j95m03ifq_flt.fits	8	448.007	882.326	0.185	0.221	-2.06276	-0.62551	0.00566	1
ib2e01vvq_flt.fits	5	123.765	282.545	0.214	0.157	-2.01437	-0.03480	0.00769	1
ib2e01vzq_flt.fits	5	118.189	292.040	0.333	0.340	-2.22402	-0.40136	0.01377	1
ib2e01ycq_flt.fits	5	211.923	288.885	0.254	0.264	1.52205	-0.39597	0.01060	1
ib2e01ygq_flt.fits	5	223.548	278.331	0.267	0.280	1.97209	0.00478	0.01120	1
ib2e02z2q_flt.fits	9	273.772	278.188	0.371	0.370	1.68974	1.10145	0.01517	1
icwp02bkq_flt.fits	6	205.306	248.166	0.319	0.319	-1.95850	-0.43190	0.01307	1
icwp02bmq_flt.fits	4	202.914	251.862	0.235	0.234	-1.98575	-0.59932	0.00961	1
icwp02bpq_flt.fits	4	216.003	288.864	0.334	0.352	-1.15706	-1.64517	0.01406	0
icwp02bsq_flt.fits	4	222.415	290.299	0.256	0.299	-0.89630	-1.60745	0.01141	1
icwp03diq_flt.fits	4	311.938	256.894	0.244	0.267	2.01320	0.96442	0.01049	1
icwp03dkq_flt.fits	4	312.991	252.780	0.369	0.368	1.96711	1.12438	0.01511	1
icwp03dpq_flt.fits	4	318.726	252.905	0.179	0.173	1.89482	1.30463	0.00721	1
icwp03dsq_flt.fits	4	317.262	248.766	0.316	0.303	1.75932	1.42066	0.01269	1
icwp04iiq_flt.fits	4	313.246	255.311	0.132	0.132	1.90648	1.25177	0.00541	1
icwp04ikq_flt.fits	4	313.561	251.962	0.158	0.162	1.83752	1.36575	0.00656	1

Extended Data Table 4 | Astrometry of Thalassa used in this study

Reference image	Coadded images	*X*	*Y*	σ(*X*) (arcsec)	σ(*Y*) (arcsec)	ΔRA (arcsec)	Δdec (arcsec)	σ(RA,dec) (arcsec)	Weight
j95m03ibq_flt.fits	1	452.570	708.050	0.207	0.246	2.18925	0.25131	0.00630	1
j95m03icq_flt.fits	1	450.060	707.417	0.189	0.167	2.19508	0.32573	0.00503	1
j95m03idq_flt.fits	1	446.729	707.269	0.369	0.372	2.18602	0.42052	0.01038	0
j95m03ieq_flt.fits	1	445.690	706.471	0.120	0.114	2.20143	0.45442	0.00329	1
j95m03ifq_flt.fits	1	442.806	706.208	0.257	0.265	2.19686	0.53727	0.00730	1
j95m03igq_flt.fits	1	439.939	706.776	0.459	0.443	2.17220	0.61485	0.01267	1
j95m03ihq_flt.fits	1	438.984	707.417	0.152	0.207	2.15303	0.63809	0.00499	1
j95m03iiq_flt.fits	1	436.773	708.102	0.248	0.251	2.12802	0.69650	0.00699	1
j95m07z6q_flt.fits	6	543.482	441.860	0.181	0.180	-2.14122	-0.16289	0.00505	1
j95m07zfq_flt.fits	6	532.141	434.603	0.207	0.153	-2.22883	-0.53702	0.00517	1
j95m08sbq_flt.fits	6	553.995	465.439	0.234	0.175	-1.82988	0.22746	0.00586	1
j95m09waq_flt.fits	6	536.564	442.856	0.125	0.121	-2.23233	-0.45639	0.00344	1
j95m09wjq_flt.fits	6	523.964	442.452	0.202	0.199	-2.14883	-0.80527	0.00561	1
j95m11gjq_flt.fits	6	546.232	621.772	0.164	0.165	1.79739	1.12473	0.00461	1
j95m11gsq_flt.fits	6	556.022	602.124	0.259	0.252	1.27404	1.24627	0.00717	1
ib2e01x6q_flt.fits	2	122.835	290.368	0.305	0.305	-2.04674	-0.14178	0.01249	1
ib2e01x8q_flt.fits	2	119.757	295.609	0.160	0.176	-2.16246	-0.34411	0.00688	1
ib2e01xaq_flt.fits	2	117.744	300.722	0.175	0.161	-2.23585	-0.54272	0.00689	1
ib2e01xcq_flt.fits	2	117.662	305.781	0.104	0.112	-2.23225	-0.74163	0.00442	1
ib2e02zjq_flt.fits	2	280.969	277.010	0.179	0.165	2.02383	1.15780	0.00705	1
ib2e02zlq_flt.fits	2	279.429	272.482	0.116	0.090	1.86089	1.26017	0.00426	0
ib2e02znq_flt.fits	2	276.168	267.615	0.134	0.125	1.63349	1.33294	0.00531	1
ib2e02zpq_flt.fits	2	271.794	262.780	0.143	0.145	1.37067	1.37890	0.00590	1
icwp01n2q_flt.fits	1	208.309	255.801	0.261	0.249	-1.14859	-1.56240	0.01045	1
icwp01n4q_flt.fits	1	212.482	258.664	0.452	0.455	-0.94360	-1.53605	0.01859	1
icwp02bjq_flt.fits	1	315.262	243.467	0.172	0.166	2.02944	1.27790	0.00693	1
icwp02bkq_flt.fits	1	314.670	242.205	0.156	0.182	1.98666	1.31537	0.00695	1
icwp02blq_flt.fits	1	314.508	240.644	0.085	0.106	1.95484	1.36970	0.00400	1
icwp02bmq_flt.fits	1	314.475	239.259	0.176	0.196	1.93071	1.41945	0.00764	1
icwp02bnq_flt.fits	1	313.208	238.340	0.126	0.116	1.86864	1.43503	0.00496	1
icwp03dhq_flt.fits	1	196.463	257.217	0.182	0.180	-2.05748	-1.10052	0.00742	1
icwp03diq_flt.fits	1	195.852	258.792	0.120	0.149	-2.04716	-1.16541	0.00554	1
icwp03djq_flt.fits	1	195.283	260.019	0.143	0.150	-2.04240	-1.21763	0.00601	1
icwp03dkq_flt.fits	1	195.007	261.482	0.126	0.113	-2.02252	-1.27273	0.00490	1
icwp03dlq_flt.fits	1	194.908	262.850	0.138	0.139	-1.99831	-1.32142	0.00568	1
icwp03doq_flt.fits	1	200.513	269.359	0.116	0.124	-1.94608	-1.36257	0.00492	1
icwp03dpq_flt.fits	1	200.688	270.321	0.126	0.134	-1.92042	-1.39247	0.00533	1
icwp03dqq_flt.fits	1	201.049	271.947	0.175	0.181	-1.87476	-1.44183	0.00730	1
icwp03drq_flt.fits	1	201.461	273.652	0.461	0.446	-1.82570	-1.49300	0.01858	1
icwp03dsq_flt.fits	1	203.097	274.701	0.141	0.132	-1.74671	-1.49990	0.00559	1
icwp03dtq_flt.fits	1	203.580	276.156	0.146	0.144	-1.70021	-1.54123	0.00594	1
icwp04ihq_flt.fits	1	208.455	240.659	0.063	0.124	-1.92613	-0.51981	0.00402	1
icwp04iiq_flt.fits	1	206.621	242.222	0.272	0.278	-1.95002	-0.60904	0.01127	1
icwp04ijq_flt.fits	1	205.173	242.908	0.308	0.311	-1.98189	-0.66195	0.01268	1
icwp04ikq_flt.fits	1	202.971	244.164	0.188	0.155	-2.02530	-0.74922	0.00705	1
icwp04ilq_flt.fits	1	201.350	245.436	0.132	0.131	-2.04901	-0.82459	0.00539	1
icwp04imq_flt.fits	1	207.665	274.393	0.155	0.171	-1.42948	-1.56516	0.00669	1
icwp04inq_flt.fits	1	209.020	275.628	0.136	0.138	-1.35514	-1.57572	0.00561	1
icwp04ioq_flt.fits	1	211.138	276.852	0.175	0.179	-1.25569	-1.56963	0.00725	1
icwp04ipq_flt.fits	1	212.932	277.637	0.282	0.234	-1.17742	-1.55641	0.01060	1
icwp04iqq_flt.fits	1	214.845	279.193	0.210	0.207	-1.07691	-1.56532	0.00854	1
icwp04irq_flt.fits	1	220.034	279.113	0.858	0.763	-0.90628	-1.45186	0.03325	1

Extended Data Table 5 | Candidate Voyager images of Hippocamp

Image	*X*	*Y*	Inside?	Exposure Time (s)	Phase Angle (°)	Range (km)
C1121132.IMG	246	965	N	61.44	14.382	8,772,700
C1121139.IMG	260	950	N	61.44	14.386	8,769,200
C1121214.IMG	827	919	N	61.44	14.412	8,751,400
C1121221.IMG	839	900	N	61.44	14.419	8,747,700
C1121346.IMG	436	561	Y	61.44	14.530	8,700,300
C1121353.IMG	443	534	Y	61.44	14.541	8,696,100
C1121428.IMG	986	448	N	61.44	14.603	8,674,400
C1121435.IMG	992	418	N	61.44	14.617	8,669,900
C1121741.IMG	401	661	Y	61.44	15.045	8,529,400
C1121744.IMG	398	647	Y	61.44	15.053	8,526,800
C1121747.IMG	392	46	Y	61.44	15.060	8,524,200
C1121750.IMG	388	32	Y	61.44	15.068	8,521,600
C1121759.IMG	999	539	N	61.44	15.090	8,513,600
C1121802.IMG	996	525	N	61.44	15.098	8,510,900
C1121805.IMG	989	-37	N	15.36	15.106	8,507,800
C1121808.IMG	986	-51	N	15.36	15.114	8,505,100
C1131016.IMG	-106	170	N	15.36	16.292	3,940,700
C1133210.IMG	360	929	N	3.84	15.039	2,981,700
C1133624.IMG	82	804	N	3.84	16.589	2,719,300
C1133630.IMG	39	772	Y	3.84	16.613	2,712,500

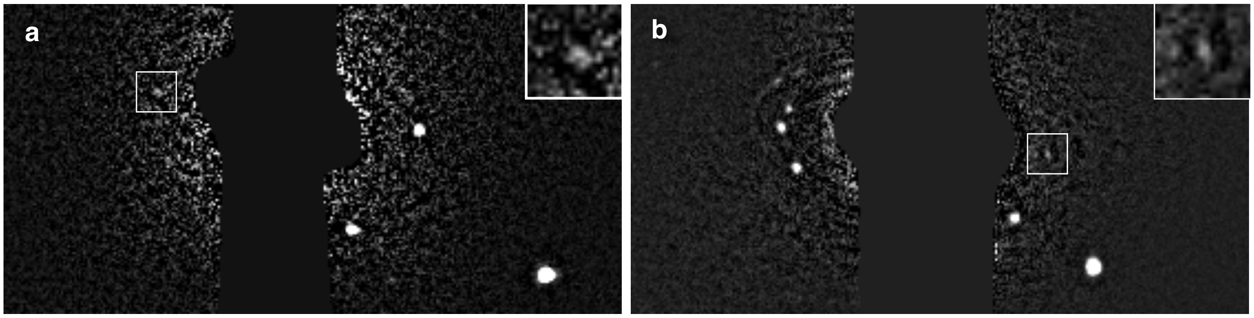

Extended Data Fig. 1 | Recovery of Naiad. Each panel shows a portion of an HST image after processing and coadding as described in the text. The location of Naiad in each panel is indicated by a small square; a closeup is inset at upper right. **a**, View from Visit 01, orbit 1 of HST program GO-11656, obtained on 2009 Aug 19. It shows the first unambiguous detection of Naiad since the 1989 Voyager flyby of Neptune. **b**, View from Visit 08, orbit 2 of program GO-14217, taken on 2016 Sep 2.

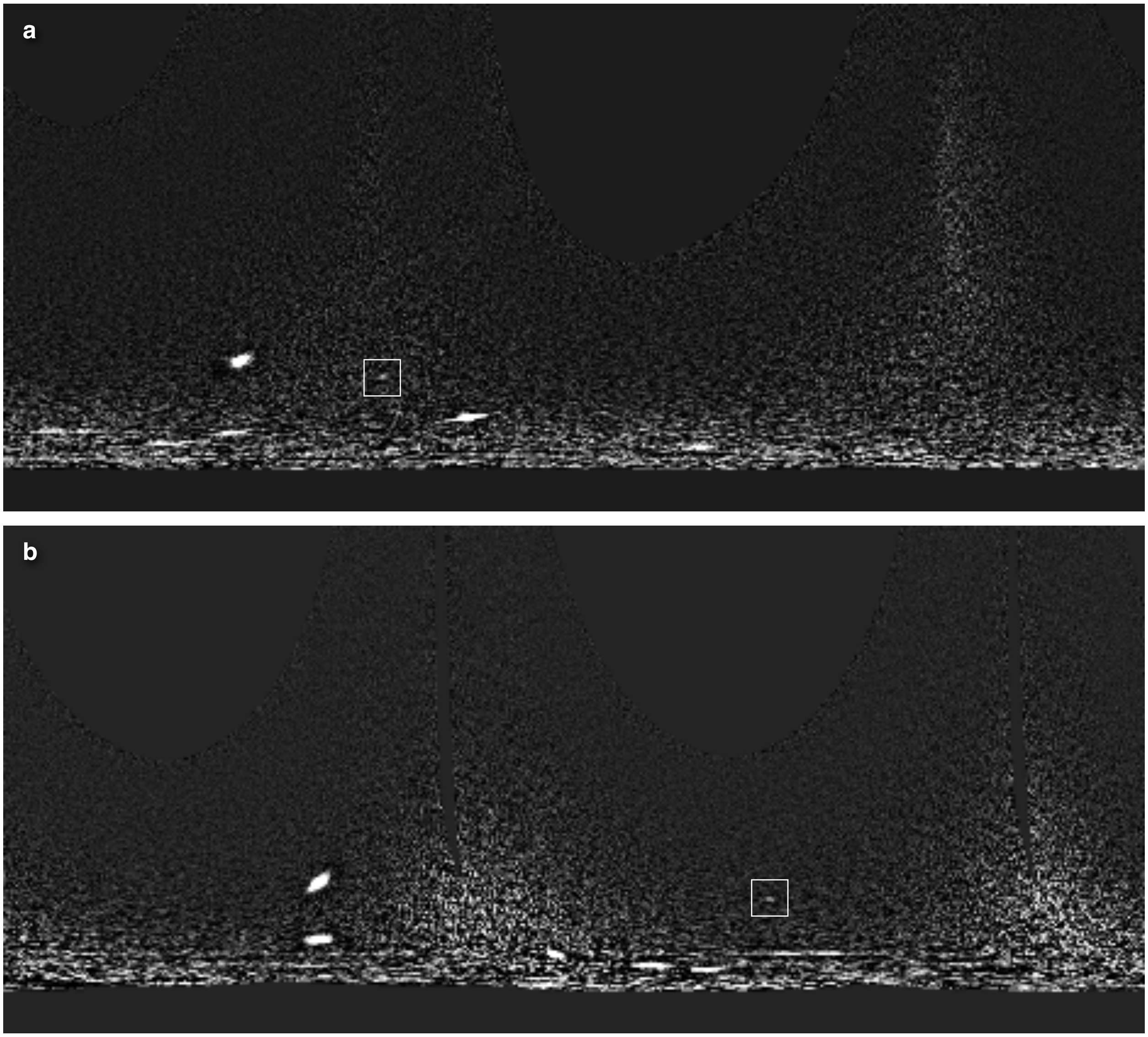

Extended Data Fig. 2 | Deep searches for small moons. Each panel shows multiple HST images coadded into a “map” in which longitude increases from 0 to 360° along the horizontal axis and radial position is 0 to 400,000 km along the vertical axis. Boxes indicate the locations of Hippocamp. **a**, View derived from the five HST orbits of program GO-11656, obtained on 2009 August 19. **b**, View from the two orbits of Visit 03 in HST program GO-14217, taken on 2016 Sep 2.

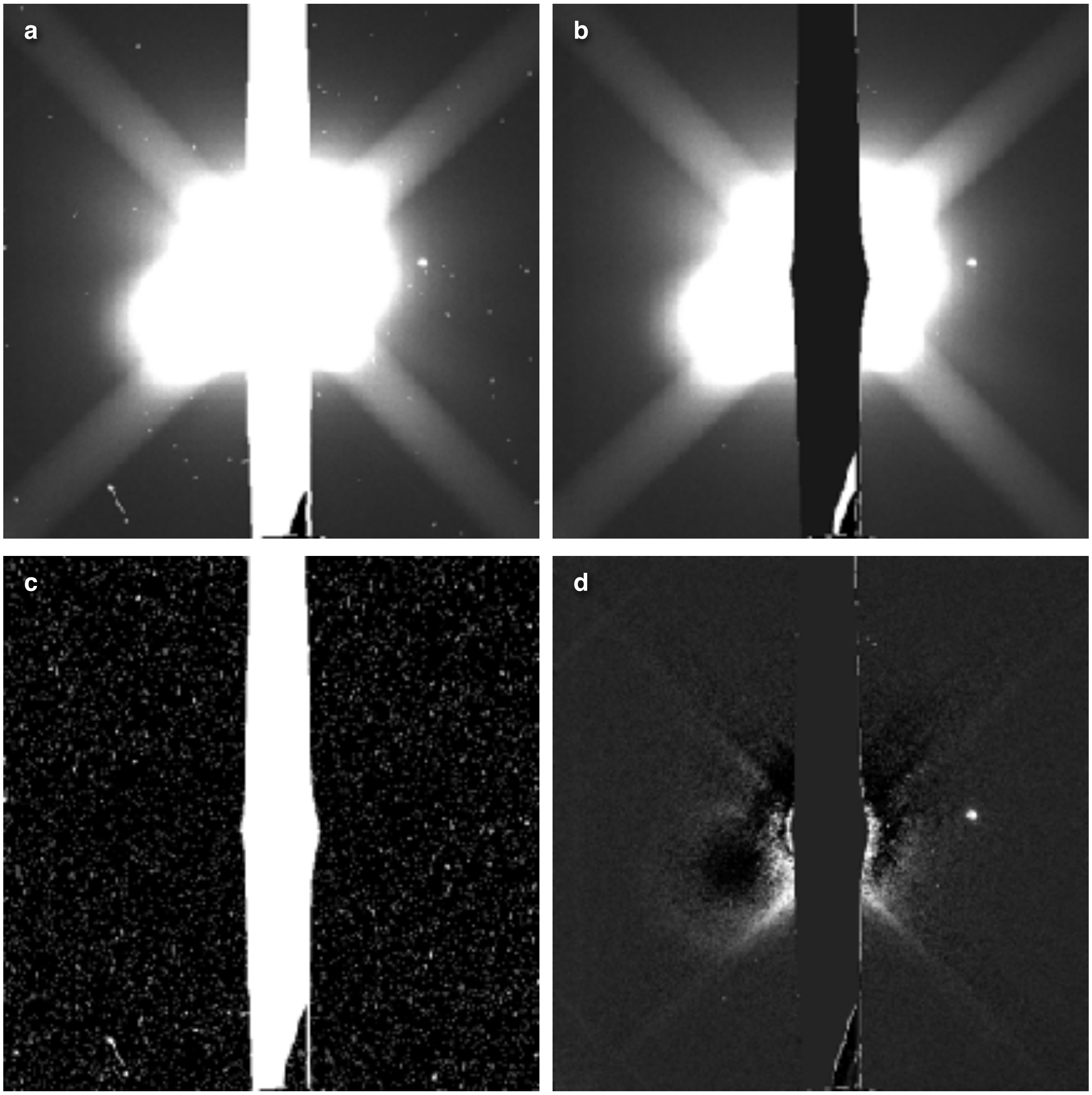

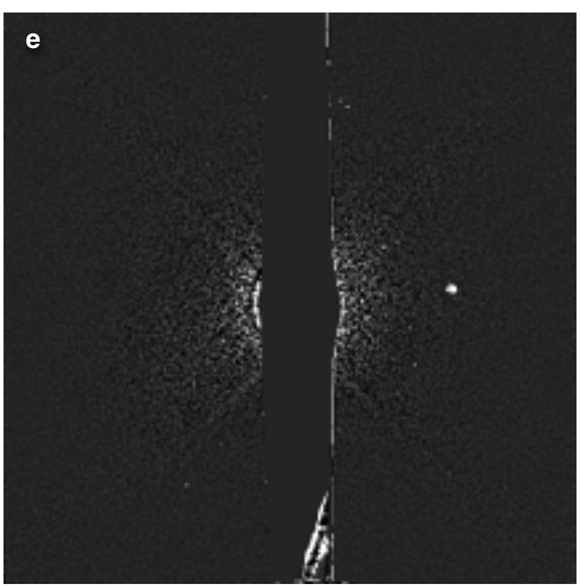

Extended Data Fig. 3 | Image processing steps illustrated. a, Image icwp01n7q_flt.fits taken on 2016 August 31. **b**, The same image after hot pixels and cosmic ray hits have been removed. **c**, The boolean mask where white indicates pixels that will be ignore from further analysis. **d**, The image after the mean of other images from the same HST visit have been averaged and subtracted. This step removes most of the glare. **e**, The image after an "unsharp mask" process involving the subtraction of a median-filtered version of the same image.

Supplementary_Table_1.xls | HST images used in this study

A spreadsheet identifying every image used in this study along with associated metadata including filter, time, and the derived location of Neptune.

Supplementary_Table_2.xls | Astrometry obtained for this study

A spreadsheet containing all our astrometric measurements of Despina, Galatea, Larissa, Proteus and Triton.

Supplementary_Video.mov | Hippocamp with Proteus

This six-frame movie shows Hippocamp just to the left of Proteus during Visit 01, orbit 2 of program GO-14217 on 2016 August 31. The proximity of Proteus, moving in the same direction and at nearly the same speed, guides the eye and makes it possible to see the much smaller moon. Hippocamp remains below the threshold for reliable detection in the individual frames but, in effect, nearby Proteus enables the human eye to do the necessary coadding. A closeup of the area inside the white square, containing both moons, is inset at lower left.